




Influence of thallium doping on structural, electrical, and optical properties of ZnO nanorods for TCO applications

Hakan Çolak^{1,2,*}  and Halil İbrahim Mercan¹

¹ Faculty of Science, Department of Chemistry, Cankiri Karatekin University, 18100 Cankiri, Türkiye

² Central Research Laboratory (CANKAM), Cankiri Karatekin University, 18100 Cankiri, Türkiye

Received: 8 February 2022

Accepted: 8 May 2022

Published online:

26 May 2022

© The Author(s), under exclusive licence to Springer Science+Business Media, LLC, part of Springer Nature 2022

ABSTRACT

Thallium (Tl)-doped ZnO nanorods were prepared (the doping ratios were between 0 and 5 mol %) in two stages. Combined sol–gel and spin-coating methods and hydrothermal method were used, respectively. Depending on the concentrations of the Tl dopant, the structural, morphological, electrical, and optical properties of the samples were examined. XRD results demonstrated that the ZnO samples were in hexagonal (wurtzite) unit cell type with single crystalline nature. FE-SEM results indicated that the undoped and Tl-doped ZnO samples had hexagonal rod-like structures. The average lengths and diameters of the samples were between 0.90 and 1.35 μm , and 80 and 120 nm, respectively. The electrical conductivity increased with increasing temperature and doping concentrations. For the undoped and 5 mol % Tl-doped ZnO-samples, the electrical conductivity values were $1.22\text{E}-08$ and $1.95\text{E}-05$ $(\Omega\cdot\text{cm})^{-1}$ at 25 °C and $4.84\text{E}-07$ and $3.97\text{E}-04$ $(\Omega\cdot\text{cm})^{-1}$ at 300 °C, respectively. The 1 mol % Tl-doped ZnO had the highest transmittance (within the range of 70 and 80%) in the wavelength of between 500 and 1000 nm. The band gap energy values of the Tl-doped samples were higher than the undoped ZnO sample.

1 Introduction

In systems with technological and industrial applications such as solar cells, optoelectronic devices generally require the use of a transparent electrode. For this purpose, n-type transparent conductive oxide (TCO) semiconductors that have high optical transmittance and electrical conductivity, and high thermal and chemical stability are preferred [1].

Fluorine-doped SnO_2 (FTO), and tin-doped In_2O_3 (ITO) are the most known and preferred TCO materials. However, ITO has some disadvantages such as low stability, toxicity, limited indium sources, as well as high cost. On the other hand, the use of indium-free FTO films is more limited due to the low conductivity and chemical stability of this material compared to ITO [2]. Fortunately, zinc oxide (ZnO) is a promising alternative TCO material. ZnO-based

Address correspondence to E-mail: hakancolak@karatekin.edu.tr

materials can be produced more economically and easily, have attracted attention recently. Thanks to its chemical and thermal stability, ZnO is a suitable material for optoelectronic device applications [3]. ZnO is an n-type semiconductor that has a wide bandgap of 3.37 eV and a large binding energy of 60 meV at room temperature.

ZnO has good both electronic and optical properties due to the non-stoichiometry caused by inherent defects such as vacancies of oxygen (V_{O_2}) and interstitial Zn atoms in the unit cell. However, these properties are not stable as atmospheric oxygen is adsorbed onto the ZnO surface, and there is a decrease in conductivity. It is necessary the impurity doping to stabilize ZnO and to further develop its properties [4]. The doping process happens in the form of the displacement of the ions of the doping element with Zn^{2+} ions which are in the unit cell of the ZnO. When ions that have higher valence than Zn^{2+} enter the unit cell, there is an increase in electron concentration in the ZnO crystal lattice and, as a result, an increase in electrical conductivity [5]. ZnO materials can be doped with a wide variety of elements of group I (Li), and of groups III or V (Al, Ga, In, N, P, As, Sb, etc.) [6]. B, Al, Ga, In as dopant materials for ZnO have attracted much attention in recent years. But there are fewer reports for other trivalent dopant materials. As an alternative TCO material, Sc, Y, La, Tl-doped ZnO samples are promising [7]. Thallium (Tl) is a group III element, too. Tl has been widely used as a dopant in scintillators applications [8]. The Tl metal enters into the ZnO crystal lattice as Tl^{+3} and has one more oxidation state than Zn^{2+} . Therefore, Tl is thought to be a suitable dopant for ZnO. However, an experimental study on Tl-doped ZnO has not been found in the literature, but there is only one theoretical study [7].

For synthesizing one dimensional (1D) ZnO nanostructures and doping impurities into them chemical vapor deposition methods such as metal-organic vapor phase epitaxy (MOVPE) [9, 10], chemical vapor deposition (CVD) [11], vapor-liquid-solid phase (VLS) [12] have been used. Compared to the vapor methods, the solution usage methods are preferred due to their simplicity, suitability for large-scale production, high product yield, and low working temperature [9]. Among the solution usage methods, the hydrothermal method developed by Vayssieres is the more accepted [13]. Via the hydrothermal approach, vertically and well-aligned

doped ZnO nanorod arrays can be synthesized, and size and morphology control can be easily made by means of synthesis conditions and chemical species used. Using simple equipment, the hydrothermal approach enables the efficient synthesis of ZnO nanorod arrays at low temperatures. In the hydrothermal method, a self-catalytic ZnO seed layer plays as the nucleus for the growth of the ZnO nanorods [14]. The ZnO seed layer is produced using sputtering [15], atomic layer deposition [16], pulsed laser deposition [17], metal-organic- CVD [18], sol-gel [19, 20] methods. Among them, the sol-gel technique is the simplest and has the ability to control particle size and morphology via systematic monitoring of reaction parameters.

2 Materials and methods

2.1 Producing the samples

Pristine and Tl-doped ZnO nanorods were produced. In the first stage, ZnO seed layers were prepared on the pre-cleaned glass substrate via combined sol-gel and spin coating routes. All chemicals used were commercially purchased. The coating solution was prepared by dissolving zinc acetate dihydrate [$Zn(Ac)_2 \cdot 2H_2O$, Sigma-Aldrich, 99–102%] in 2-methoxyethanol [$C_3H_8O_2$, Sigma-Aldrich, $\geq 99.3\%$]. Then, monoethanolamine [MEA, C_2H_7NO , Merck, $\geq 99.5\%$] was added into the solution as a stabilizer. The concentration of the coating solution was adjusted at 0.5 M and the molar ratio of MEA to Zn^{2+} was 1:1. A 1 mL volume of the solution was dropped with a micropipette on the glass substrate, which was rotated at 3000 rpm for 30 s using the spin-coating system. The obtained films were pre-heated at 250 °C for 15 min to remove organic residues. The coating and pre-heating cycles were repeated five times to get a ZnO seed layer of appropriate thickness. Subsequently, the seeded glass was heated at 450 °C for 12 h (h) to complete crystallization. In the second stage, for the growth of undoped and Tl^{3+} -doped ZnO nanorods on the seeded glass substrates, an aqueous solution of zinc nitrate hexahydrate [$Zn(NO_3)_2 \cdot 6H_2O$, Sigma-Aldrich, $\geq 99.0\%$] with concentration of 0.075 M, hexamethylenetetramine [HMTA, $C_6H_{12}N_4$, Sigma-Aldrich, $\geq 99.5\%$] was prepared. The molar ratio of HMTA with Zn^{2+} was 1:1. Then thallium nitrate trihydrate [$Tl(NO_3)_3 \cdot 3H_2O$,

Sigma-Aldrich] was added to the aqueous solution as a dopant source, at different concentrations of 1, 2, 3, 4, and 5 mol %. The mixture was transferred into a teflon-lined autoclave reactor. The hydrothermal process was achieved by keeping the temperature of the reactor at 95 °C for 4 h.

2.2 Characterizations

Structural, morphological, electrical conductivity, and optical transmittance characteristics of the samples were studied. The structural analysis was investigated by powder X-Ray Diffraction (XRD) using copper $\text{CuK}\alpha$ radiation ($\lambda = 1.5406 \text{ \AA}$) (PANalytical EMPYREAN) along with the diffractometer equipped with a diffracted beam graphite monochromator, copper X-ray tube. The diffraction data were collected in the 2θ range of 5° – 90° with a step size of 0.02, and a count time of 50 s per step at 45 kV and 40 mA. The morphological characteristic was examined by a field emission scanning electron microscope (FE-SEM) (Zeiss, Gemini 500) operated at an accelerating voltage of 20 kV, equipped with energy-dispersive X-ray spectroscopy (EDX). The Four-probe technique was used to examine the electrical characteristic of the samples. The measurements were achieved under the air atmosphere by using a Keithley 2400 source meter at temperatures between 25 and 300 °C. For this purpose, a measuring system of our own design was used and the samples were placed down in the center of the system. Platinum wires used to reduce the contact resistance were attached to the sample surface so that they were symmetrical in the center of the sample and the distances between the wires were 0.2 cm.

Using the following formula the dc electrical conductivity (σ) was calculated:

$$\sigma = \frac{I}{V} G^{-1}, \quad (1)$$

where I is the measured current, V is the potential voltage, and G is the geometric structure factor [21]. When calculating the resistivity, a correction element should be used that changes according to the geometry of the sample and the positions of the contacts on the sample. Considering these ratios for sample sizes of $t/s \geq 0.5$ and $d/s < 40$, the G factor can be calculated as follows:

$$G = 2\pi s F_1(t/s) F_2(d/s). \quad (2)$$

In this equation:

$$F_1\left(\frac{t}{s}\right) = \frac{\frac{t}{s}}{2 \ln\left(\frac{\sinh\left(\frac{t}{s}\right)}{\sinh\left(\frac{t}{2s}\right)}\right)} = \frac{0.5}{2 \ln\left(\frac{\sinh(0.5)}{\sinh(0.25)}\right)} = 0.35, \quad (3)$$

$$F_2\left(\frac{d}{s}\right) = \frac{\ln 2}{\ln 2 + \ln\left(\frac{\left(\frac{d}{s}\right)^2 + 3}{\left(\frac{d}{s}\right)^2 - 3}\right)} = \frac{\ln 2}{\ln 2 + \ln\left(\frac{(6.5)^2 + 3}{(6.5)^2 - 3}\right)} = 0.83. \quad (4)$$

The variation of the electrical conductivity against temperature was examined by the Arrhenius equation:

$$\sigma = \sigma_0 \exp\left[-\frac{E_a}{kT}\right], \quad (5)$$

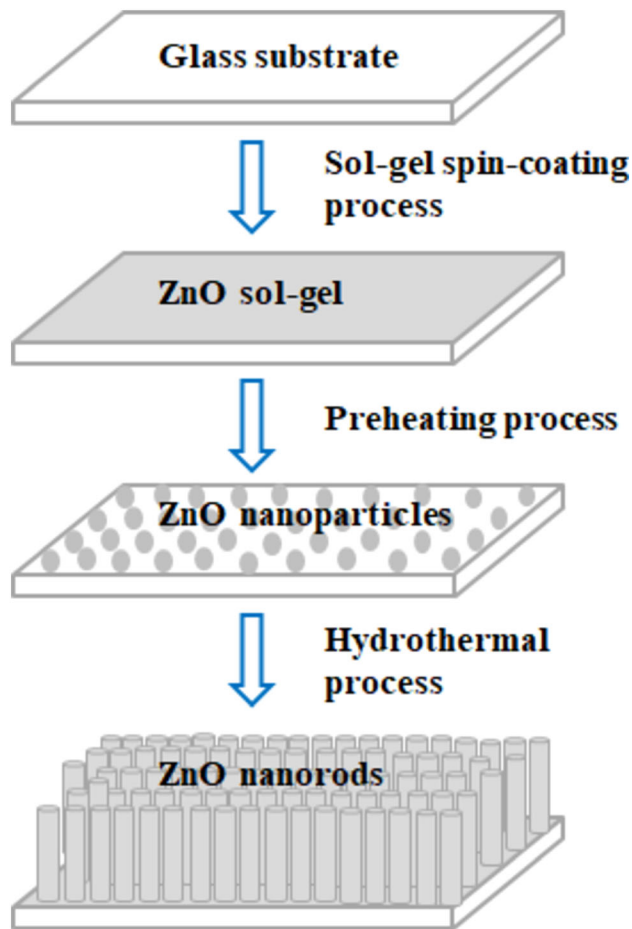
where σ_0 , E_a , k , and T are the pre-exponential factor, the activation energy, the Boltzmann constant, and the temperature (in Kelvin), respectively [22].

The optical properties were investigated in a wavelength range of 300–1000 nm by a double-beam spectrophotometer with a spectral bandwidth of 1 nm at room temperature using. For this aim, Rayleigh—Model UV2601 UV/VIS spectrophotometer was used Scheme 1.

3 Results and discussions

3.1 XRD and FE-SEM analysis

Figure 1 demonstrates the XRD patterns of the obtained samples. The (002) peaks in the patterns have the highest intensity and indicate that the samples have the hexagonal wurtzite structure with single-crystalline nature, and nanorods grow along the c -axis. In the XRD pattern of the undoped sample (002) and (004) diffraction peaks are seen. Also, the very low intensity of the ground radiation and the absence of impurity peaks in the pattern of the undoped sample indicate that the crystal quality of the sample is high (Fig. 1a). In addition to these peaks, the Ti^{3+} -doped ZnO samples have peaks of (100), (101), (102), (110), (103), (200), (112), (201), (202), (104), and (203) (Fig. 1b and c). The patterns are a very good match with the standard data (JCPDS number 36-1451). No impurity or secondary phase has been observed. Also, it is seen that the intensity of



Scheme 1 Schematic diagram of the undoped and Tl-doped ZnO nanorods production

the (002) peaks decreases with the increase of the doping amount in the XRD patterns of the Tl-doped samples. The peak with the highest intensity is (101) in the XRD pattern of the 5 mol% Tl-doped ZnO sample. In this pattern, it is observed that the main growth orientation of the crystal is not the *c*-axis, but different orientations. The decrease in the peak intensities and the increase in the ground radiation intensities indicate that the crystal quality decreases. As seen in Fig. 1d, a shift in the positions of the (002) peaks toward higher two thetas (2θ) diffraction angle with the increasing of the Tl doping amount has been observed. Table 1 listed the calculated *a* and *c* unit cell constants of the ZnO. Both constants increase as increasing the amount of the Tl doping. The ionic radii (six-coordinated) of the Tl^{3+} and Zn^{2+} ions are 0.89 and 0.74 Å, respectively [23]. The doping process happens by substituting Zn^{2+} ions in the ZnO sites with Tl^{3+} ions. This increase in the constants as the

doping amount increases can be explained by the difference between the radius of the Zn^{2+} and Tl^{3+} ions [24, 25]. The shift of the (002) peak positions and the increase in the constants clearly pointed out that the Tl^{3+} ions substituted the Zn^{2+} sites in the ZnO unit cell. A similar trend was reported by another study [26].

For the ZnO samples, the average crystallite sizes (*D*) were estimated via the Scherrer formula from the (002) peaks [27]:

$$D = \frac{K\lambda}{\beta \cos\theta}, \quad (6)$$

where *D* is the average crystallite size, λ is the x-ray wavelength, β is the width of the x-ray peak on the 2θ axis, normally measured as full width at half maximum (FWHM) after the error due to instrumental broadening has been properly corrected (subtraction of variances), θ is the Bragg angle, and *K* is the so-called Scherrer constant (~ 0.9). There is no significant correlation between the doping concentration versus the crystallite size (Table 1).

Figure 2 demonstrates the FE-SEM micrographs of the ZnO nanorods produced with various Tl^{3+} doping amounts. The undoped ZnO sample has hexagonal-shaped rod structures with smooth surfaces Fig. 2a. The average width and length of the undoped ZnO nanorods are 100 nm and 1.0 μm , respectively. Also, the Tl^{3+} -doped ZnO samples have hexagonal rod-like structures Fig. 2b–f. The average lengths and diameters of the Tl^{3+} -doped ZnO samples are between 0.90 and 1.35 μm , and 80 and 120 nm, respectively (Table 1). There is no regular variation between the average diameter of the nanorods versus the doping concentration. While the nanorods are better aligned in the vertical direction for the 1 and 2 mol % doped ZnO samples, the vertical alignment is disrupted after 3 mol %. As the doping concentration increases, the nanorod structure and crystal quality begin to deteriorate. The EDX and elemental mapping analysis confirmed the Tl content of the ZnO samples. The results are demonstrated in Fig. 3. The EDX results indicate that Tl^{3+} ions enter into the crystal structure. Also, the mapping results show that Tl^{3+} ions are distributed homogeneously overall material, which also confirmed the formation of Tl^{3+} -doped ZnO nanorods. According to the EDX results, the doping concentrations of the Tl^{3+} ions that have entered into the ZnO crystal lattice are given in Table 2.

Fig. 1 **a** XRD pattern of the undoped ZnO nanorods; **b** and **c** XRD patterns of the Tl-doped ZnO nanorods; **d** shifts in the (002) peak position of the ZnO nanorods

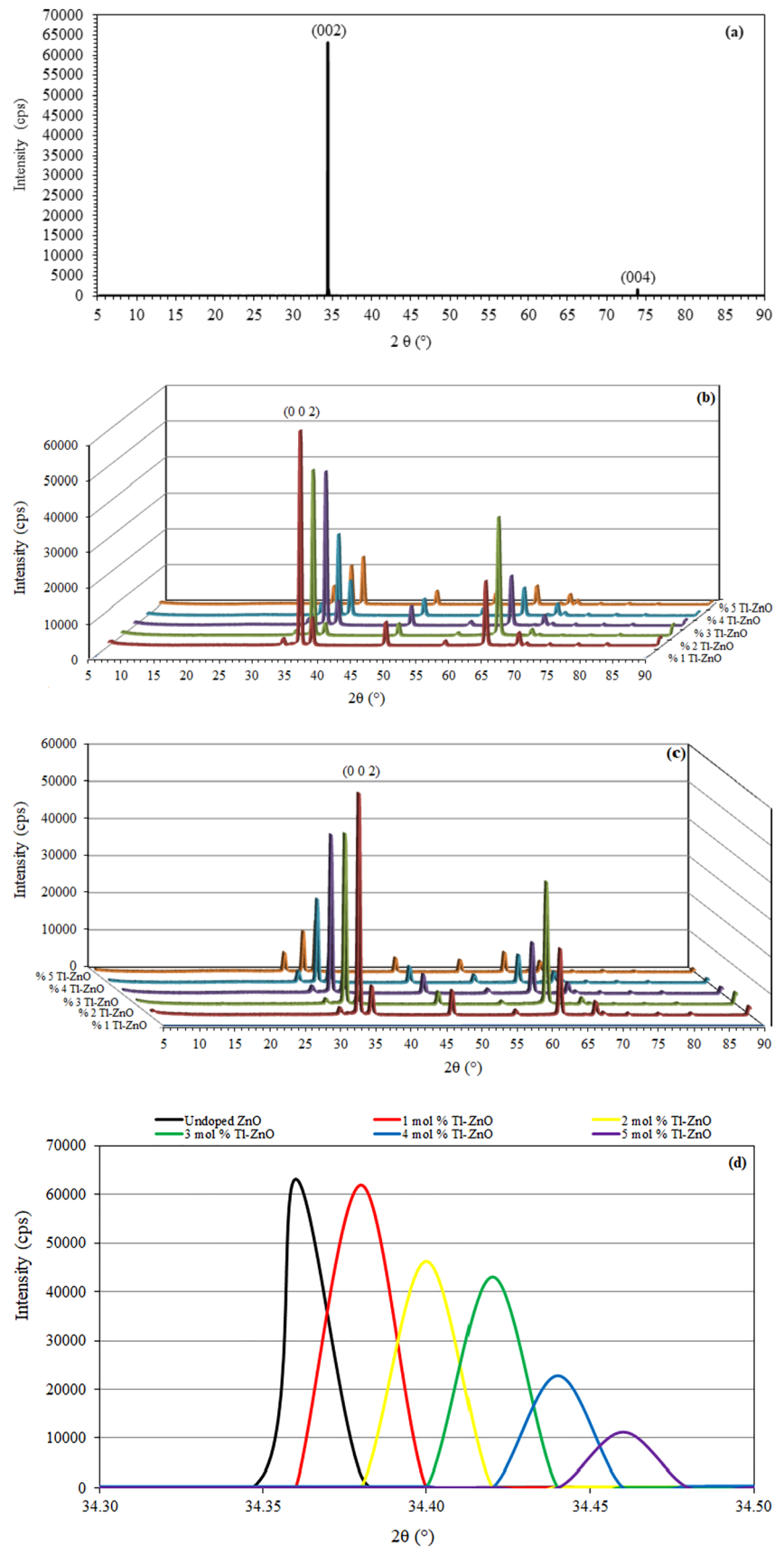
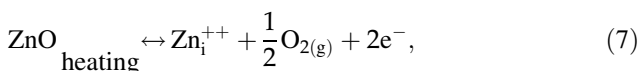


Table 1 The values of the unit cell constants, activation energy, bandgap energy, crystallite size, and average diameter of the ZnO nanorods samples

Samples	Lattice constants, (Å)		Activation energy, (eV)		Optical bandgap energy, E_g (eV)	Average crystallite size, D (nm)	Average diameter of the rod, (nm)
	a	c	E_{a_1} (25–150 °C)	E_{a_2} (150–300 °C)			
Undoped ZnO	–	5.1500	–	–	3.20	25	100
% 1 Tl-ZnO	3.2490	5.2052	0.06	0.29	3.23	24	100
% 2 Tl-ZnO	3.2497	5.2048	0.07	0.24	3.24	24	90
% 3 Tl-ZnO	3.2527	5.2055	0.08	0.32	3.22	23	105
% 4 Tl-ZnO	3.2575	5.2080	0.04	0.29	3.23	24	110
% 5 Tl-ZnO	3.2609	5.2114	0.06	0.24	3.20	25	120

3.2 DC electrical measurements

The crystal structure of the ZnO samples has an effect on the electrical conductivity. The heat treatment modifies the crystal structure of the ZnO samples, and accordingly in the electrical conductivity properties [28]. The electrical conductivity depending on the temperature was measured, and $\log\sigma - 1000/T$ graphs of the ZnO samples were plotted. The graphs are grouped for comparison in Fig. 4. As understood from the figure, as a requirement of semiconducting behavior, the electrical conductivity of the pure and doped ZnO samples increases with increasing heat treatment temperature. The following reaction equation can explain the increase in electrical conductivity of pure ZnO sample with the increase in temperature:



where Zn_i^{++} is the interstitial Zn^{2+} ion. The conductivity of ZnO increases after the ionization resulting from the heat treatment, two electrons are released, so the amount of free charge carriers increases, and accordingly [29]. Also, as the oxygen molecules adsorbed onto the ZnO surface will be desorbed from the ZnO surface at high temperatures, the potential barrier height at the grain boundaries decreases, and accordingly the electrical conductivity increases. In addition, intrinsic imperfections such as oxygen deficiency (V_{O_2}) which formed donor levels below the conduction band in the forbidden zone and caused the conduction mechanism are resulting in the electrical conductivity of the pristine ZnO. The Tl amount and the produced imperfections control the electrical conductivity mechanism. The increase in the electrical conductivity with Tl amount means that

the doping process influences the imperfection chemistry of the ZnO [30]. The carrier concentration in the ZnO unit cell increases with Tl doping concentration because Tl^{3+} has one more valence electron than Zn^{2+} . Thus, the Tl^{3+} -doped samples have higher electrical conductivity than the pure ZnO. The values of the electrical conductivity at different temperatures are given in Table 3.

The activation energy (E_a) was found via the following formula:

$$\sigma = \sigma_{\text{Low}} \exp\left[\frac{E_{a(\text{Low})}}{kT}\right] + \sigma_{\text{High}} \exp\left[\frac{E_{a(\text{High})}}{kT}\right]. \quad (8)$$

In this equation, $\sigma_{\text{Low}} - \sigma_{\text{High}}$ and $E_{a(\text{Low})} - E_{a(\text{High})}$ demonstrate the electrical conductivity and activation energy for the conduction mechanisms in the low- and high-temperature zones, respectively. With increasing temperature, the electrical conductivity increases slowly in the low-temperature zone (25–150 °C). The migrating of the carriers within localized levels may cause this slow increase in the electrical conductivity. The electrical conductivity increases with increasing temperature in the high-temperature zone (150–300 °C) [31]. The slope of the linear part of the $\log\sigma - 1000/T$ graph is equal to $-E_a/k$. The E_a values were calculated for the samples from the curves, and given in Table 1. It is understood that the E_a values increase in both low and high-temperature zones with the increase of the doping concentration. The Tl atoms may generate the structural changes or supply new acceptor/donor levels [32]. The Tl atoms replacing with Zn^{2+} ions and occupying the zinc interstitial site are thought to either have a higher ionization potential or be a deep donor (or act as). Therefore, the Tl atoms can not be

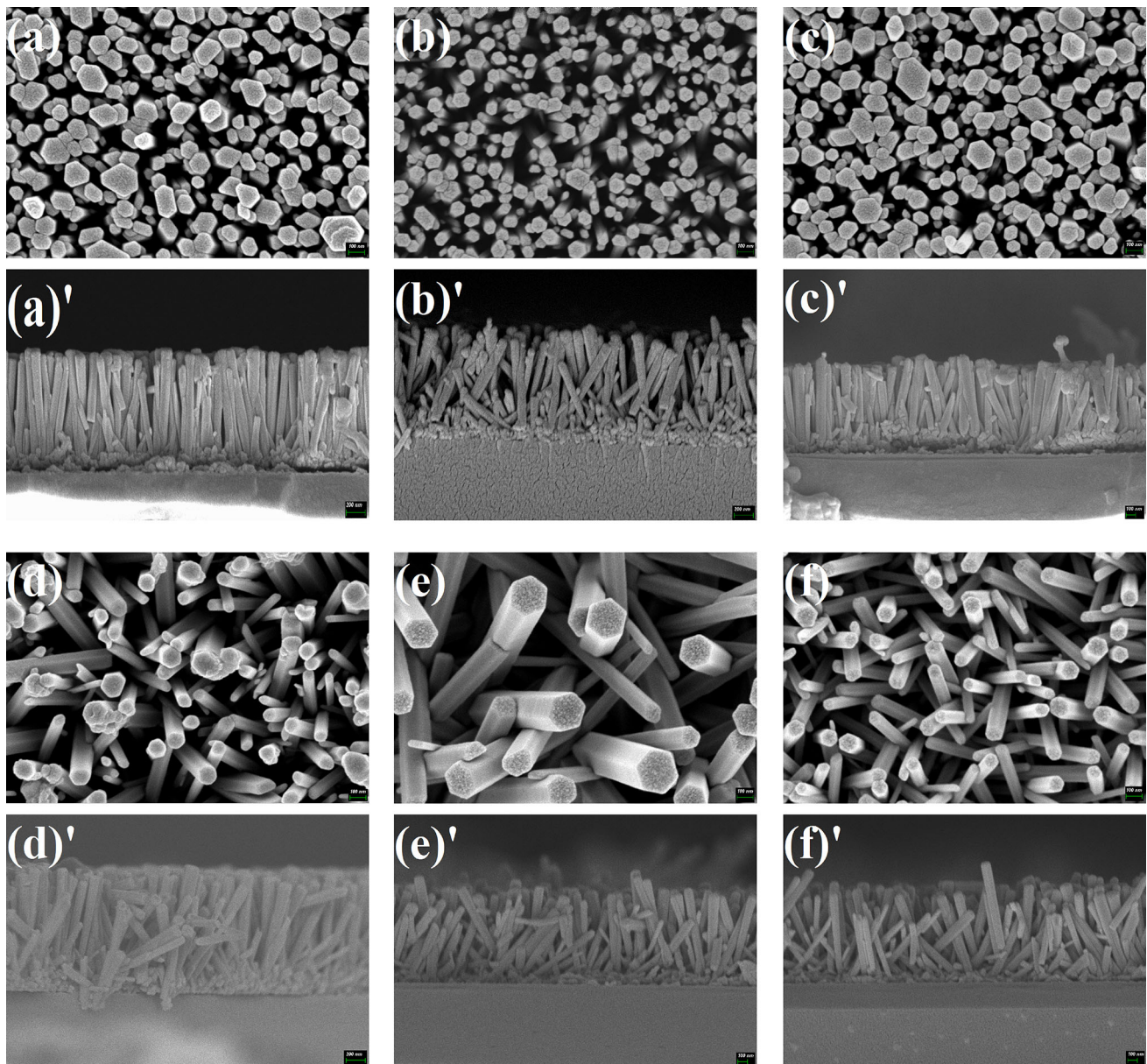


Fig. 2 Top view and cross sectional FE-SEM images of the ZnO samples: **a-a'** undoped; **b-b'** 1 mol %; **c-c'** 2 mol %; **d-d'** 3 mol %; **e-e'** 4 mol %; and **f-f'** 5 mol % Tl-doped

ionized as easily as the Zn atoms [33]. It is understood from Table 1 that the E_a values in the low-temperature zone are less than those in the high-temperature zone due to the changing the conductivity mechanism from one to another within the material. The electrical conductivity which is called intrinsic conductivity is mainly controlled by intrinsic imperfections in the high-temperature zone. The high values of the E_a in this zone may be due to the fact that the energy required to generate the imperfections is greater than the energy needed for its

entrapment. Therefore, the intrinsic imperfections caused by thermal differences control the high-temperature electrical conductivity of the samples [34].

3.3 Optical characterization

The optical absorption spectra for all the ZnO samples were taken in the range of 300–1000 nm using a UV–Visible double-beam spectrophotometer. The spectra are demonstrated in Fig. 5. The results indicate that the optical transmittance increases with

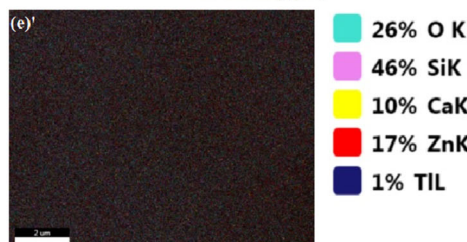
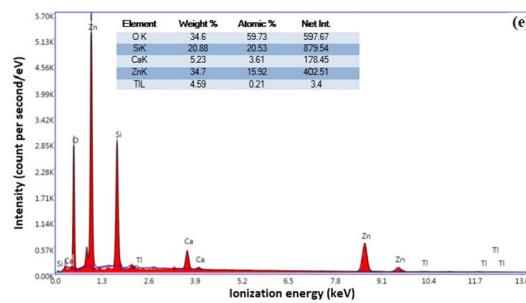
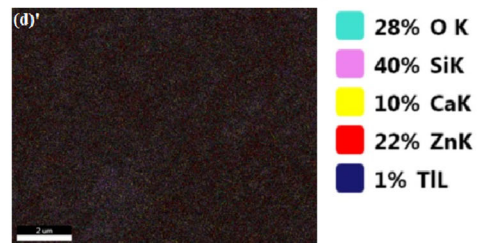
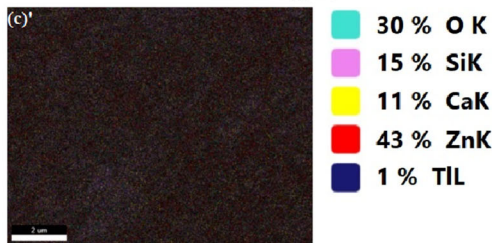
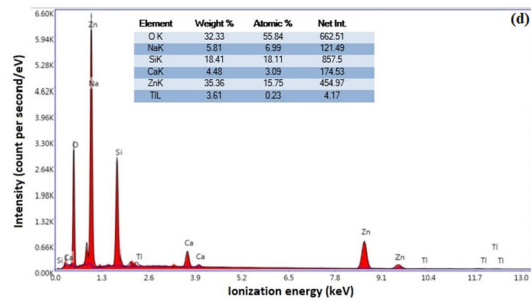
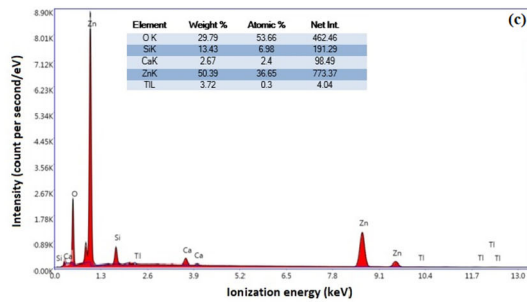
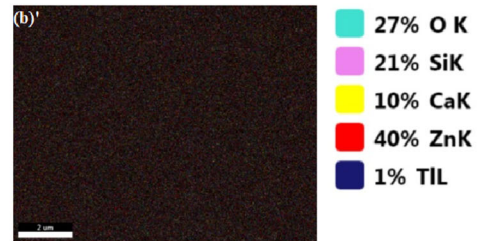
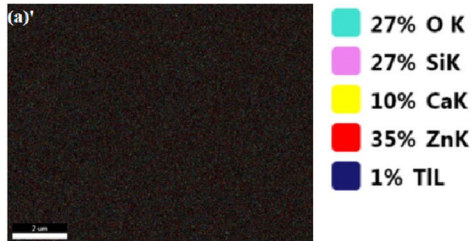
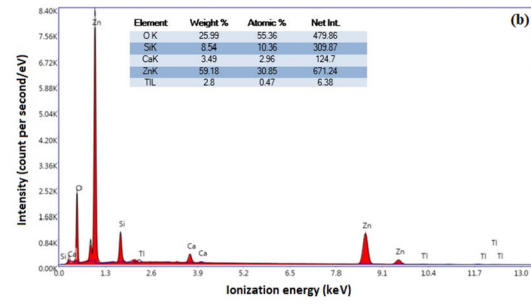
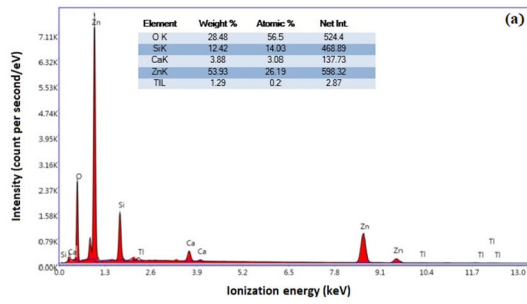


Fig. 3 EDX spectra and elemental mapping images of the Tl ZnO samples: **a-a'** 1 mol %; **b-b'** 2 mol %; **c-c'** 3 mol %; **d-d'** 4 mol %; and **e-e'** 5 mol % Tl-doped

increasing thallium doping concentration. The sample with 3 mol % Tl-doped has the highest optical transmittance in the range of 350–1000 nm (within the range of 70 and 80%). The 4 mol % Tl-doped sample shows the lowest transmittance in the range of 350–675 nm. However, at longer wavelengths, the samples with 4 and 5 mol % Tl-doped have higher optical transmittance than undoped ZnO. This result

may be attributed to the reduction of the defects in the sample and the improvement of the homogeneous structure with uniformly spread out particles. So, the increased optical transmittance may be due to the crystallinity of the samples [35].

The optical band gap energy (E_g) of the ZnO samples was determined using Tauc formula [36]:

$$\alpha(h\nu) = A(h\nu - E_g)^n, \quad (9)$$

where $\alpha(h\nu)$ is the absorption factor, h is the Planck constant, A is a constant, ν is the wave frequency, and $n = 1/2$, for a direct semiconductor.

Table 2 The EDX results of Tl³⁺-doped ZnO samples

Tl ³⁺ doping concentration, (Theoretically calculated value before starting the experiment) $\left(\frac{\text{mol number of Tl}^{3+}}{\text{mol number of Zn}^{2+}} \times 100\right)$	Tl ³⁺ doping concentration, (Value obtained from EDX results after the experiment) $\left(\frac{\text{mol number of Tl}^{3+}}{\text{mol number of Zn}^{2+}} \times 100\right)$
1	0.76
2	1.51
3	2.36
4	3.26
5	4.14

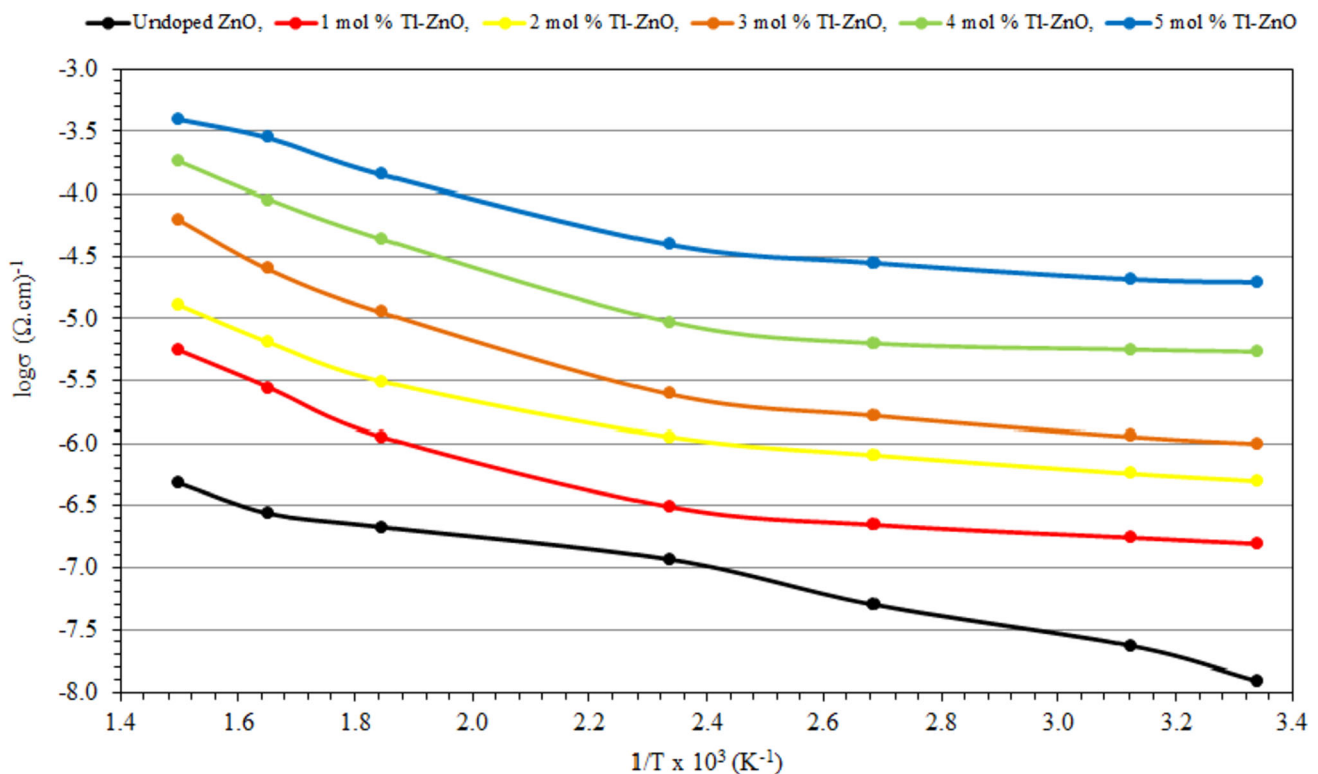


Fig. 4 A combined demonstration of the electrical conductivity variations of all the ZnO samples for comparison

Table 3 The values of the electrical conductivity of the ZnO samples at different temperatures

Tl doping amount (mol %)	Electrical conductivity values, σ ($\Omega\cdot\text{cm}$). ⁻¹						
	25(°C)	50(°C)	100(°C)	150(°C)	200(°C)	250(°C)	300(°C)
Undoped	1.22 E-08	2.32 E-08	4.98 E-08	1.15 E -07	2.12 E -07	2.73 E -07	4.84 E -07
1	1.22 E-08	2.32 E-08	4.98 E-08	1.16 E-07	2.13 E-07	2.73 E-07	4.85 E-07
2	4.99 E-07	5.73 E-07	8.05 E-07	1.13 E-06	3.11 E-06	6.45 E-06	1.29 E-05
3	9.99 E-07	1.14 E-06	1.66 E-06	2.47 E-06	1.12 E-05	2.50 E-05	6.29 E-05
4	5.35 E-06	5.58 E-06	6.24 E-06	9.22 E-06	4.29 E-05	8.97 E-05	1.79 E-04
5	1.95 E-05	2.07 E-05	2.80 E-05	3.93 E-05	1.42 E-04	2.81 E-04	3.97 E-04

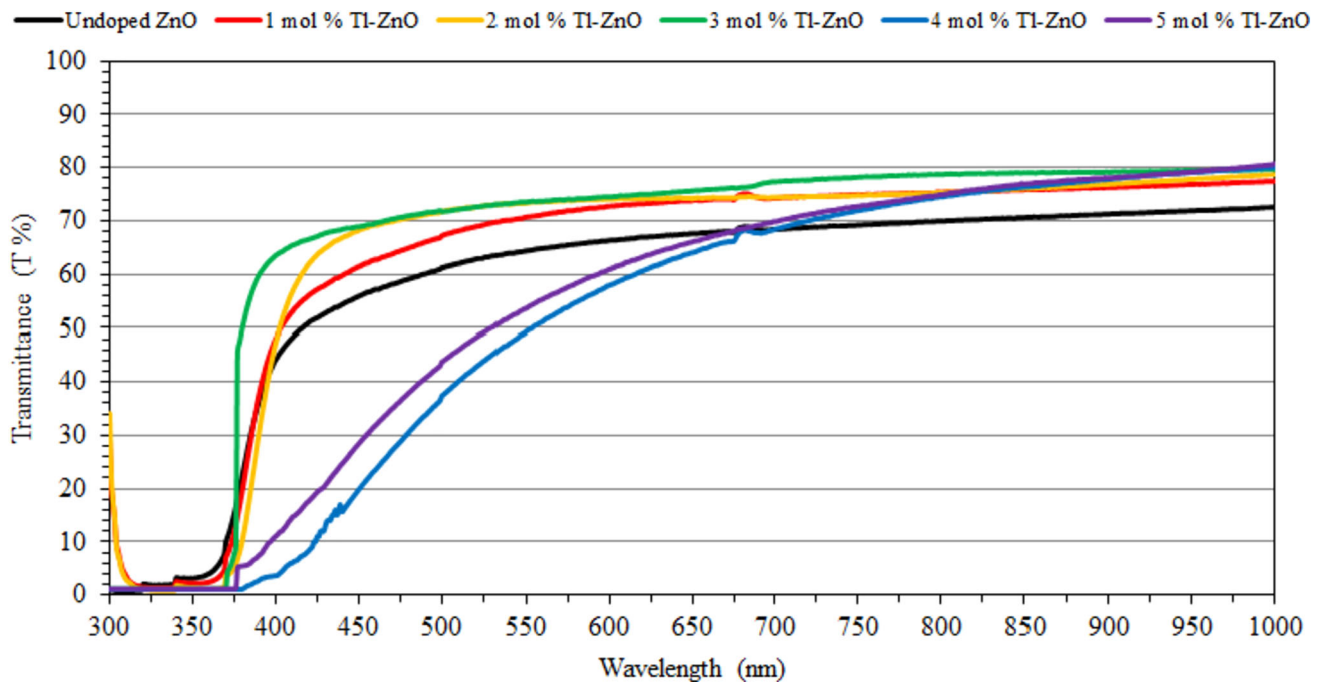


Fig. 5 Optical transmittance graphs of the ZnO samples

Figure 5 shows the Tauc plots that are the energy ($h\nu$) versus $(\alpha h\nu)^2$ for the pure and Tl-doped ZnO samples. In order to have detailed information about the values of the optical band gap energy of the samples, the dependence of the absorption factor on the photon energy in the high absorption region was investigated. The E_g values are found by extrapolating and intersecting the linear portion of $(\alpha h\nu)^2$ to the energy axis (Fig. 6). Based on the calculations, the results are listed in Table 1. The optical band gap energy values of the Tl-doped samples are mostly higher than the undoped ZnO sample, however, there is no regular variation between themselves of the doped samples. The broadening in the optical band gap with the increase of dopants concentrations

can be explained by the changes in the lattice constants. This change significantly modifies the electronic levels of the samples. Therefore, the redistribution of energy bands is directly associated with the structure (unit cell constants) of the samples. Thus, the variations in the unit cell constants change the band gap values [37]. Our result is consistent with the results of the other works. Chen et al. produced La-doped ZnO samples via sol-gel and spin-coating methods. They observed that the bandgap of La-doped ZnO samples increases with the increasing doping amounts [38]. Serrao et al. deposited pure and Sn-doped ZnO samples on the glass substrates via spin-coating method, and observed an increase in the optical band gap while increasing Sn doping amount

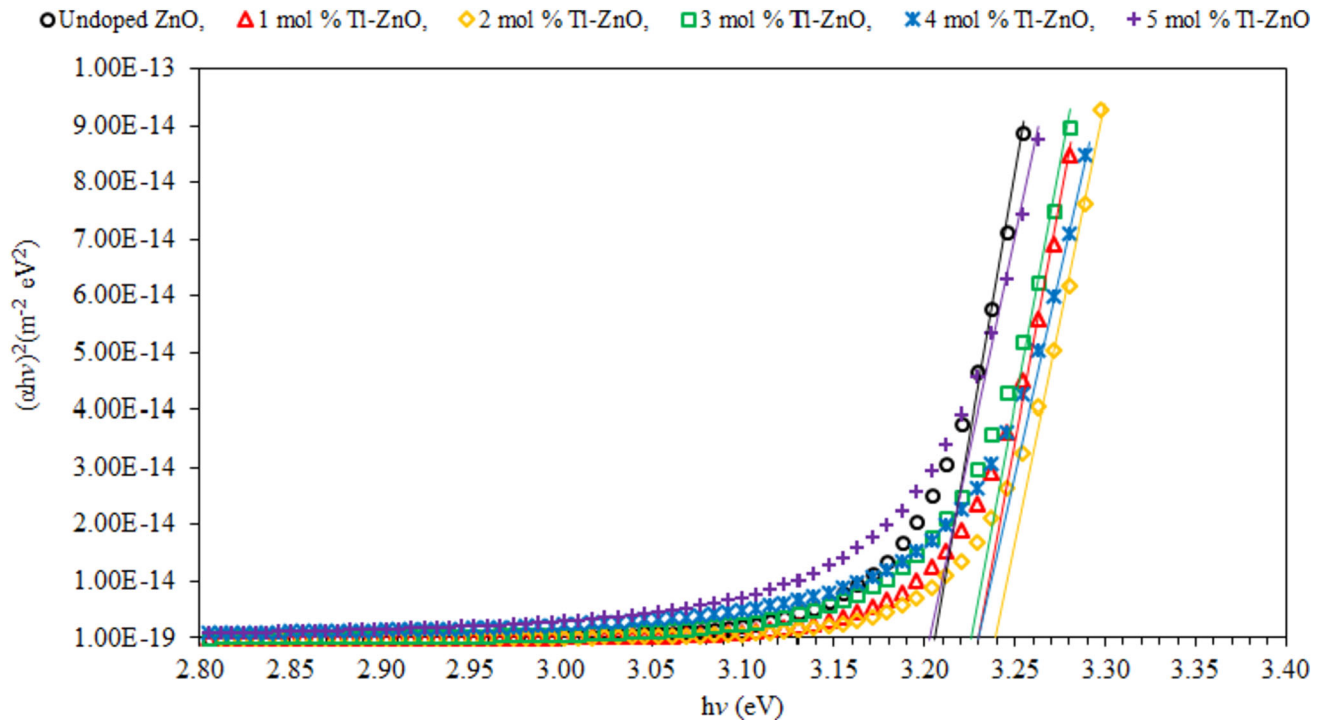


Fig. 6 Graphs of $(\alpha hv)^2$ vs energy ($h\nu$) of the ZnO samples

[37]. Kovalenko et al. determined in their theoretical study that with increasing Al, Ga, In, and Tl doping concentration there was an increase in the optical band gap [7].

4 Conclusion

In this study, the pristine and Tl-doped ZnO nanorods were fabricated. The unit cell constants increased with increasing dopant concentrations. There was a red shifting in the locations of the (002) peak in the XRD patterns as the doping concentrations increased. The FE-SEM results demonstrated that the samples had rod-like structure, and the nanorod arrays were vertically aligned on the substrate. The electrical conductivity of the samples increased with increasing temperature and Tl doping concentrations. The optical measurements indicated that the undoped ZnO sample had the highest transmittance in between 500 and 1000 nm. The E_g values of the Tl-doped samples were higher than the undoped ZnO sample. The deterioration in crystal quality of the ZnO samples with the Tl doping seen in the XRD patterns, and the variations in the nanorod orientations seen in the FE-SEM micrographs, and the irregular changes in the optical transmittance support

each other. The optical transmittance can be improved by coating the thin film on the surface of the glass substrate is more homogeneously and by making the nanorod orientations in the c -axis direction more uniform. With increasing doping concentration, also, variations which are in the unit cell constants calculated from XRD data, in the values of the electrical conductivity, and in the bandgap confirm the existence of Tl^{3+} ions and their entry into the ZnO crystal lattice. In this way, Tl-coated ZnO nanorods samples can be considered as an alternative TCO material.

Authors contribution

HÇ: investigation, writing—original manuscript, supervision. HİM: investigation.

Data availability

The datasets generated during and/or analyzed during the current study are available from the corresponding author on reasonable request.

Declarations

Conflict of interest Authors declare that there are no conflict of interest.

References

- S. Sohn, Y. Soo Han, Transparent conductive oxide (TCO) films for organic light emissive devices (OLEDs) organic light emitting diode- material, process and devices. IntechOpen (2011). <https://doi.org/10.5772/18545>
- M.A. Auouaj, R. Diaz, A. Belayachi, F. Rueda, M. Abd-Lefdil, Comparative study of ITO and FTO thin films grown by spray pyrolysis. *Mater Res Bull* **44**, 1458–1461 (2009). <https://doi.org/10.1016/j.materresbull.2009.02.019>
- Y. Liu, Y. Li, H. Zeng, ZnO-based transparent conductive thin films: doping, performance, and processing. *J. Nanomater.* (2013). <https://doi.org/10.1155/2013/196521>
- H. Çolak, O. Türkoğlu, Studies on structural and electrical properties of copper-doped zinc oxide powders prepared by a solid state method at high temperatures. *Mater. High Temp.* **29**, 344–350 (2012). <https://doi.org/10.3184/096034012X13390873728509>
- V. Kumari, V. Kumar, B.P. Malik, R.M. Mehra, D. Mohan, D. Mohan, Nonlinear optical properties of erbium doped zinc oxide (EZO) thin films. *Opt. Commun.* **285**, 2182–2188 (2012). <https://doi.org/10.1016/J.OPTCOM.2011.12.094>
- F. Chaabouni, J.B. Belgacem, M. Abaab, Physical properties of TCO-ZnO thin films sputtered from a powder target. *Chin. J. Phys.* **52**(1), 272–285 (2014). <https://doi.org/10.1155/2015/936482>
- M. Kovalenko, O. Bovgyra, A. Franiv, V. Dzikovskyi, Electronic structure of ZnO thin films doped with group III elements. *Mater. Today-Proc.* **35**, 604–608 (2019). <https://doi.org/10.1016/j.matpr.2019.11.274>
- R. Hofstadter, Alkali halide scintillation counters. *Phys. Rev.* **74**, 100–101 (1948). <https://doi.org/10.1103/PhysRev.74.100>
- N. Huang, M.W. Zhu, L.J. Gao, J. Gong, C. Sun, X. Jiang, A template-free sol–gel technique for controlled growth of ZnO nanorod arrays. *Appl. Surf. Sci.* **257**, 6026–6033 (2011). <https://doi.org/10.1016/j.apsusc.2011.01.112>
- K. Ogata, K. Maejima, F. Sz, S.G. Fujita, Growth mode control of ZnO toward nanorod structures or high-quality layered structures by metal-organic vapor phase epitaxy. *J. Cryst. Growth* **248**, 25–30 (2003). [https://doi.org/10.1016/S0022-0248\(02\)01843-2](https://doi.org/10.1016/S0022-0248(02)01843-2)
- J.J. Wu, S.C. Liu, Low-temperature growth of well-aligned ZnO nanorods by chemical vapor deposition. *Adv. Mater.* **14**, 215–218 (2002). <https://doi.org/10.1002/1521-4095>
- J. Zhao, L. Qin, L. Zhang, Synthesis of quasi-aligned Si-doped ZnO nanorods on Si substrate. *Physica E* **40**, 795–799 (2008). <https://doi.org/10.1016/j.physe.2007.10.057>
- L. Vayssieres, Growth of arrayed nanorods and nanowires of ZnO from aqueous solutions. *Adv. Mat.* **15**, 464–466 (2003). <https://doi.org/10.1002/adma.200390108>
- P.N. Mbuyisa, O.M. Ndwandwe, C. Cepek, Controlled growth of zinc oxide nanorods synthesized by the hydrothermal method. *Thin Solid Films* **578**, 7–10 (2015). <https://doi.org/10.1016/j.tsf.2015.02.002>
- L.W. Brooks, J.M. Mativetsky, A. Woll, D. Smilgies, Y.L. Loo, Sputtered ZnO seed layer enhances photovoltaic behavior in hybrid ZnO/P3HT solar cells. *Org. Electron.* (2013). <https://doi.org/10.1016/j.orgel.2013.09.023>
- S.Y. Pung, K.L. Choy, H.X. Shan, C. Preferential growth of ZnO thin films by the atomic layer deposition technique. *Nanotechnology* (2008). <https://doi.org/10.1088/0957-4484/19/43/435609>
- S. Saini, P. Mele, H. Honda, T. Suzuki, K. Matsumoto, K. Miyazaki, A. Ichinose, L.M. Luna, R. Carlini, A. Tiwari, Effect of self-grown seed layer on thermoelectric properties of ZnO thin films. *Thin Solid Films* **605**, 289–294 (2016). <https://doi.org/10.1016/j.tsf.2015.09.060>
- H.G. Chen, Z.W. Li, Seed-assisted growth of epitaxial ZnO nanorod arrays with self-organized periodicity and directional alignment. *Appl. Surf. Sci.* **258**, 556–564 (2011). <https://doi.org/10.1016/j.apsusc.2011.08.069>
- J. Zhang, W. Que, Preparation and characterization of sol–gel Al-doped ZnO thin films and ZnO nanowire arrays grown on Al-doped ZnO seed layer by hydrothermal method. *Sol. Energ. Mat. Sol. C* **94**, 2181–2186 (2010). <https://doi.org/10.1016/j.solmat.2010.07.009>
- Y.C. Yoon, K.S. Park, S.D. Kim, Effects of low preheating temperature for ZnO seed layer deposited by sol–gel spin coating on the structural properties of hydrothermal ZnO nanorods. *Thin Solid Films* **597**, 125–130 (2015). <https://doi.org/10.1016/j.tsf.2015.11.040>
- S. Yilmaz, The geometric resistivity correction factor for several geometrical samples. *J. Semicond.* **36**(082001), 2015 (2015). <https://doi.org/10.1088/1674-4926/36/8/082001>
- H. Çolak, O. Turkoglu, Structural and electrical properties of V-doped ZnO prepared by the solid state reaction. *J. Mater. Sci- Mater. El* **23**, 1750–1758 (2012). <https://doi.org/10.1007/s10854-012-0657-1>
- RC Weast. *Handbook of Chemistry and Physics*, 56nd ed. (Newyork, Crc Pres., pp. F-198–199, 1975–1976.
- S. Goel, N. Sinha, H. Yadav, S. Godara, A.J. Joseph, B. Kumar, Ferroelectric Gd-doped ZnO nanostructures: enhanced dielectric, ferroelectric and piezoelectric properties.

- Mater. Chem. Phys. **202**, 56–64 (2017). <https://doi.org/10.1016/j.matchemphys.2017.08.067>
25. H. Çolak, O. Türkoğlu, Effect of doping and high-temperature annealing on the structural and electrical properties of $Zn_{1-x}Ni_xO$ ($0 \leq x \leq 0.15$) powders. *J. Mater. Sci. Tech.* **27**, 944–995 (2012). <https://doi.org/10.1007/s10854-012-0657-1>
 26. H. Çolak, E. Karaköse, Electrical and optical properties of well aligned Ho^{3+} -doped ZnO nanorods as an alternative transparent conducting oxide. *J. Min. Met. Mat. S* **73**, 395–403 (2021). <https://doi.org/10.1007/s11837-020-04483-z>
 27. P. Scherrer, Bestimmung der Grösse und der inneren Struktur von Kolloidteilchen mittels Röntgenstrahlen. *Nachr Ges Wiss Göttingen* **26**, 98–100 (1918)
 28. A. Jimenez-Gonzalez, S. Suarez-Parra, Effect of heat treatment on the properties of ZnO thin films prepared by successive ion layer adsorption and reaction (SILAR). *J. Cryst. Growth* **167**, 649–655 (1996). [https://doi.org/10.1016/0022-0248\(96\)00308-9](https://doi.org/10.1016/0022-0248(96)00308-9)
 29. A. Janotti, C.G. Van de Walle, Fundamentals of zinc oxide as a semiconductor. *Rep. Prog. Phys.* **72**, 126501 (2009). <http://doi.org/10.1088/0034-4885/72/12/126501>
 30. M. Behrens, G. Lolli, N. Muratova, I. Kasatkin, M. Hävecker, R.N. d'Alnoncourt, O. Storcheva, K. Köhler, M. Muhler, R. Schlögl, The effect of Al-doping on ZnO nanoparticles applied as catalyst support. *Phys. Chem. Chem. Phys.* **15**, 1374–1381 (2013). <https://doi.org/10.1039/C2CP41680H>
 31. M.M. Rahman, M.K.R. Khan, M.R. Islam, M.A. Halim, M. Shahjahan, M.A. Hakim, D.K. Saha, J.U. Khan, Effect of Al doping on structural, electrical, optical and photoluminescence properties of nano-structural ZnO thin films. *J. Mater. Sci. Tech.* **28**, 329–335 (2012). [https://doi.org/10.1016/S1005-0302\(12\)60064-4](https://doi.org/10.1016/S1005-0302(12)60064-4)
 32. R. Bhardwaj, A. Bharti, J.P. Singh, K.H. Chae, N. Goyal, Influence of Cu doping on the local electronic and magnetic properties of ZnO nanostructures. *Nanoscale Adv.* **2**, 4450–4463 (2020). <https://doi.org/10.1039/D0NA00499E>
 33. H. Çolak, Influence of Tm_2O_3 doping on structural and electrical properties of ZnO. *J. Mater. Sci- Mater. El* **26**, 784–790 (2015). <https://doi.org/10.1007/s10854-014-2464-3>
 34. A.V. Patil, C.G. Dighavkar, S.K. Sonawane, S.J. Patil, R.Y. Borse, Effect of firing temperature on electrical and structural characteristics of screen printed ZnO thick films. *J. Optoelectron. Biomed. Mater.* **1**, 226–233 (2009)
 35. E.M. Mkawi, K. Ibrahim, M.K.M. Ali, M.A. Farrukh, A.S. Mohamed, The effect of dopant concentration on properties of transparent conducting Al-doped ZnO thin films for efficient Cu_2ZnSnS_4 thin-film solar cells prepared by electrodeposition method. *Appl. Nanosci.* **5**, 993–1001 (2015). <https://doi.org/10.1007/s13204-015-0400-3>
 36. J. Tauc, Optical properties and electronic structure of amorphous Ge and Si. *Mater. Res. Bull.* **3**, 37–46 (1968). [https://doi.org/10.1016/0025-5408\(68\)90023-8](https://doi.org/10.1016/0025-5408(68)90023-8)
 37. F.J. Serrao, N.N. Bappalige, K.M. Sandeep, S. Raghavendr, Dominance of c-axis orientation on the carrier transport properties of Sn doped ZnO thin films. *Thin Solid Films* **722**, 138579 (2021). <https://doi.org/10.1016/j.tsf.2021.138579>
 38. J.T. Chen, J. Wang, F. Zhang, G.A. Zhang, Z.G. Wu, P.X. Yan, The effect of La doping concentration on the properties of zinc oxide films prepared by the sol–gel method. *J. Cryst. Growth* **310**, 2627–2632 (2008). <https://doi.org/10.1016/j.jcrysgro.2008.01.011>

Publisher's Note Springer Nature remains neutral with regard to jurisdictional claims in published maps and institutional affiliations.